Nature Communications

https://doi.org/10.1038/s41467-026-71026-6

Article in Press

Pathogenic KIF1A R350 mutations disrupt a conserved and conformation-dependent kinesin-tubulin salt bridge

Received: 8 September 2025

Accepted: 10 March 2026

Cite this article as: Shatarupa, A., Rao, L., Asenjo, A.B. *et al.* Pathogenic KIF1A R350 mutations disrupt a conserved and conformation-dependent kinesin-tubulin salt bridge. *Nat Commun* (2026). https://doi.org/10.1038/s41467-026-71026-6

Abhipsa Shatarupa, Lu Rao, Ana B. Asenjo, Arne Gennerich & Hernando Sosa

Pathogenic KIF1A R350 Mutations Disrupt a Conserved and Conformation-Dependent Kinesin-Tubulin Salt Bridge.

Abhipsa Shatarupa[1,*], Lu Rao[1,*], Ana B. Asenjo[1], Arne Gennerich[1,#], and Hernando Sosa[1,#]

[*]These authors contributed equally.

[1]Department of Biochemistry and Gruss-Lipper Biophotonics Center, Albert Einstein College of Medicine, Bronx, NY 10461, USA.

[#]Correspondence to arne.gennerich@einsteinmed.edu, hernando.sosa@einsteinmed.edu

Abstract

Pathogenic variants in the motor domain of the kinesin-3 motor protein KIF1A cause a range of neurodevelopmental and neurodegenerative conditions collectively termed KIF1A-associated neurological disorder (KAND). Among these, mutations at residue R350 are linked to hereditary spastic paraplegia and altered motor function. Yet, the structural basis for their pathogenicity remains unclear. Here, we present high-resolution cryo-electron microscopy (cryo-EM) structures of KIF1A R350G and R350W bound to microtubules in both the apo and AMP-PNP–bound states. We identify a salt bridge between KIF1A residue R350 and α-tubulin E415 that forms only in the open conformation of the motor domain and is disrupted in both mutants. The loss of this electrostatic interaction correlates with increased velocity, reduced processivity, and decreased microtubule affinity in the open, apo conformation, as demonstrated by single-molecule assays. Our results reveal an electrostatic interaction at the motor–microtubule interface that regulates KIF1A's motility behavior.

Introduction

KIF1A is a neuron-specific motor protein that moves toward the microtubule plus end and plays an essential role in anterograde transport of synaptic vesicle precursors, dense-core vesicles and in nuclear migration during brain development[1-6, 7,8]. It belongs to the kinesin-3 family, a subgroup of the kinesin superfamily of ATP-driven molecular motors that convert the chemical energy of ATP hydrolysis into mechanical work and directional movement along microtubules[9,10]. Although KIF1A can exist as a monomer[2], cargo binding promotes its dimerization, enabling processive, hand-over-hand movement similar to that of conventional kinesin (kinesin-1)[11-13].

Mutations in the *KIF1A* gene are associated with a broad range of neurodevelopmental and neurodegenerative conditions, collectively referred to as KIF1A-associated neurological disorder (KAND)[14,15]. Most KAND-associated mutations localize to the motor domain and are believed to impair motor function by disrupting ATP hydrolysis, microtubule binding, or the coordination between KIF1A's two motor heads[14,16-21]. However, some mutations—such as V8M, A255V, and R350G—display gain-of-function features, including enhanced velocity or increased microtubule binding[22,23], and have been identified in patients with hereditary spastic paraplegia[24].

KIF1A residue R350 lies within the motor domain at the end of α-helix 6, immediately preceding the neck-linker, a ~15-residue segment whose conformational transition drives motility[25]. The phenotype associated with R350 mutations has been proposed to arise either from conformational changes in the adjacent neck-linker[24,26] or from disruption of KIF1A's autoinhibited conformation, resulting in a hyperactive motor[22]. Alternatively, this mutation may perturb key contacts between KIF1A and the microtubule, particularly the interaction between R350 in KIF1A and E415 in α-tubulin. Supporting this possibility, early low-resolution cryo-EM maps and alanine-scanning experiments identified α-helix 6 as part of the microtubule-binding interface in several kinesins[27-32]. Moreover, mutational analysis of charged tubulin residues showed that substitution of α-tubulin E415 alters the microtubule-stimulated ATPase activity of kinesin-1[33]. Complementary molecular-dynamics simulations further suggest that electrostatic interactions between R350 and several α-tubulin residues, including E415, are important for microtubule binding in the ADP state. Providing strong support for this interaction, recent high-resolution structures of KIF1A–microtubule complexes revealed that in the "open" conformation of the motor domain, observed in the apo/ADP state and in the leading head of two-head-bound intermediates, R350 is positioned close to α-tubulin E415 at a distance compatible with the formation of a salt bridge[20].

In this work, to elucidate the structural and mechanistic consequences of mutations at residue R350, we determine cryo-EM structures of KIF1A R350G and R350W mutants in the apo and AMP-PNP–bound states and perform single-molecule fluorescence assays. Our results show that both mutations disrupt a conserved salt bridge with α-tubulin, resulting in increased velocity and reduced processivity.

Results

Cryo-EM structures of KIF1A R350 mutants bound to microtubules

We determined cryo-EM structures of dimeric KIF1A (amino acids 1–393) carrying the KAND-associated R350G and R350W mutations, bound to microtubules in both the nucleotide-free (apo) state and in the presence of the non-hydrolyzable ATP analog AMP-PNP (hereafter ANP), at overall resolutions of 2.9–3.3 Å (Fig. 1, Table 1, Supplementary Fig. 1). At these resolutions, atomic models could be fitted into the maps with sub-angstrom precision for most of the protein backbone (Supplementary Fig. 2). Close-up views of the cryo-EM densities and corresponding models are shown in Supplementary Figure 3.

In the ANP-bound state, both R350 mutants adopt a two-heads-bound configuration closely resembling that of wild-type KIF1A[20] (Fig. 1a, b). The leading head assumes an open conformation with a rear-pointing (minus-end-directed) neck-linker, while the trailing head is in a closed conformation with a docked neck-linker. Clear nucleotide density is present in the active sites of both motor domains.

Within this shared two-heads-bound architecture, subtle but reproducible differences are observed between the R350G and R350W ANP-bound structures (Fig. 2, Supplementary Fig. 4). These differences include small changes in the trajectory of the backward-oriented neck linker and modest shifts in the relative position/orientation of the two motor domains. Such structural variations are consistent with differences in inter-head tension between the two mutants and suggest that the identity of residue 350 modulates mechanical coupling between the heads in the ATP-like state.

In the apo state, both mutants adopt a one-head-bound configuration, with the bound motor domain in an open conformation that closely matches apo wild-type KIF1A[20] (Fig. 1c, d). Only the initial segment of the minus-end-directed neck-linker is visible, while the remainder of the neck-linker, the neck coiled-coil, and the partner motor domain are not resolved, indicating substantial mobility of the unbound head in the absence of nucleotide.

R350 mutations selectively disrupt a salt bridge in the open conformation

The open and closed conformations of the nucleotide-binding pocket can be characterized by measuring the average distances between highly conserved kinesin residues involved in nucleotide coordination[20,34]. These distances were very similar in both conformational states for wild-type KIF1A and the R350G and R350W mutants (Fig. 3a), indicating that the nucleotide-binding geometries are largely preserved in the R350 mutants.

Structural comparison of wild-type and mutant motor domains shows that, aside from the altered residue at position 350, the motor domain structures are nearly superimposable in their respective conformations, including regions surrounding the mutation site (Fig. 3b-d). The most prominent structural difference lies in the chemical nature of residue 350 (Fig. 4). In the open conformation, the wild-type R350 resides near α-tubulin residue E415 at a distance compatible with the formation of a salt bridge (Fig. 4a, b). However, in the closed conformation, R350 is further away from α-tubulin E415 and does not contact tubulin (Fig. 4c).

In the R350G mutant, the side chain is absent, and in the R350W mutant, the positively charged arginine is replaced with a bulky hydrophobic residue. Both substitutions eliminate the open conformation salt bridge (Fig. 4d, e, g, h). Thus, these structures show that the R350 mutations prevent the formation of an open-conformation-specific KIF1A–tubulin salt bridge.

R350 mutations reduce microtubule affinity in the apo state.

Loss of the KIF1A R350 and α-tubulin E415 salt bridge is expected to weaken microtubule binding in the open conformation. To test this prediction, we measured microtubule landing rates and dwell times for apo-state KIF1A (Fig. 5), which adopts a single-head open conformation. Both R350 mutants showed markedly reduced landing rates (k_{on}) and unbinding rates (k_{off}), resulting in higher apparent dissociation constants (K_D) relative to wild type, approximately four-fold for R350G and twenty-four-fold for R350W. These findings indicate that disrupting the R350-mediated salt bridge substantially decreases KIF1A's microtubule affinity at its open conformation and that the chemical nature of the substitution (Gly versus Trp) further modulates the severity of this defect.

R350 mutations increase velocity and reduce processivity

To assess the functional consequences of the R350 mutations, we performed single-molecule motility assays to measure two key parameters of kinesin movement: velocity and run length (Fig. 6). Velocity reflects the rate of forward stepping, while run length is the average distance traveled on microtubules before detachment and serves as a proxy for processivity—the motor's ability to take multiple successive steps without dissociating.

Both R350G and R350W mutants exhibited significantly increased velocities compared to wild-type KIF1A (Fig. 6b), consistent with previous reports showing that R350G enhances stepping speed and can

rescue locomotion defects in *C. elegans* lacking the corresponding endogenous kinesin[22]. In contrast, run lengths were significantly reduced for both mutants (Fig. 6b), indicating impaired processivity. This reduction was more pronounced for R350W, likely reflecting the greater decrease in microtubule affinity observed in the open state (Fig. 5) and potentially influenced by the subtle structural differences observed in the two-heads-bound state (Fig. 2).

Together, the results indicate that disruption of the KIF1A R350 to α-tubulin E415 salt bridge lowers the energetic barrier for the open-to-closed transition, increasing stepping rate. Conversely, the absence of this salt bridge may increase the likelihood of leading head (open conformation) detachment and, consequently, the probability of both heads detaching simultaneously during translocation, resulting in reduced processivity (Fig. 7).

Discussion

Here, we solved the cryo-EM structures of dimeric, microtubule-bound KIF1A carrying disease-associated mutations at position R350 (R350G and R350W) and characterized their motility using single-molecule assays. We found that these mutations cause modest yet significant alterations in motor behavior, specifically, increased velocity and decreased processivity, due to the disruption of an electrostatic interaction between KIF1A R350 and α-tubulin residue E415.

The R350G mutation has been reported to produce a relatively mild clinical phenotype compared to other KAND-associated mutations[14], which is consistent with the subtle structural and functional changes we observed. There is less data regarding the R350W mutation, but it has been reported as a dominant mutation[35], suggesting that even moderate motility defects can manifest as disease in the heterozygous state.

We propose that the primary pathogenic mechanism of R350 mutations arises from the loss of a stabilizing salt bridge formed in the open, microtubule-bound conformation of KIF1A between R350 and α-tubulin E415. The resulting increase in motor stepping, decrease in run length, and reduced microtubule affinity in the apo (open) state indicate a lowered energetic barrier for the open-to-closed transition and an elevated likelihood of detachment during stepping. KIF1A residue R350 is located near the end of α-helix 6, at a position where a positively charged residue (arginine or lysine) is highly conserved across the kinesin superfamily (Supplementary Fig. 5), suggesting that this residue may serve a similar role in other kinesins. Computational studies have indicated that interactions between the

equivalent residue in kinesin-1 (KIF5B R321) and α-tubulin are important for microtubule binding[36], and α-tubulin residue E415 has been shown to be critical for coupling microtubule binding with kinesin-1 ATPase activation[33]. Notably, a recent study reported that the the mutation in α-tubulin 4A, E415K, results in spastic ataxia[37]. Collectively, these observations underscore how disruption of a single conserved electrostatic interaction in a specific motor-domain conformation can alter kinesin mechanochemistry and contribute to neurological disease.

An earlier hypothesis proposed that the R350G mutation alters KIF1A activity by affecting the neck-linker conformation, based on the proximity of R350 to the neck-linker[24,26]. However, this idea predated high-resolution (<4 Å) kinesin–microtubule structures[20,34] and assumed that KIF1A R350 does not interact with the microtubule, which is not the case, as highlighted in this work. Furthermore, our data show similar neck-linker conformations between wild-type and the R350G mutant in both the open and closed states, indicating no substantial structural effect of this mutation on the neck-linker.

Another possibility is that the R350G mutation activates the motor by disrupting the autoinhibited, folded conformation of full-length KIF1A, as has been proposed for other gain-of-function mutations like V8M and A255V[22]. While we cannot completely rule out this mechanism, structural considerations argue against it. A proposed structural model for kinesin-3 autoinhibition is based on the crystal structure of full-length KLP6[38]. This structure shows a compacted folded conformation of the kinesin monomer where the coiled coils and FHA (forkhead-associated domain) domains fold onto the motor domain, covering the nucleotide-binding site and preventing dimerization. In this structure, the residue equivalent to KIF1A R350 (R354 in KLP6) is located far from the regions involved in forming the folded autoinhibited state and does not contact any structural elements associated with autoinhibition (Supplementary Fig. 6a). Similarly, predicted full-length models of KIF1A using AlphaFold3[39] place R350 far from the key intramolecular interfaces involved in forming a folded autoinhibited conformation (Supplementary Fig. 6b, d, e), further supporting the conclusion that R350 is unlikely to contribute to autoinhibition. It has also been proposed that KIF1A in the autoinhibited state exists as a dimer rather than a monomer[13], but AlphaFold3 dimer models likewise place residue R350 far from the interfaces that form a folded autoinhibited state (Supplementary Fig. 6c, f, g). Taken together, these structural considerations support our conclusion that the disruption of the open-conformation KIF1A R350 to α-tubulin E415 salt bridge is the primary mechanism underlying the altered motor function of KIF1A R350 mutations.

In summary, our findings demonstrate that mutations at R350 perturb a critical salt bridge at the motor–microtubule interface, leading to enhanced velocity and reduced processivity. The fact that such subtle biophysical changes result in clinically observable motor dysfunction underscores the importance of precise kinetic and mechanical tuning in neuronal transport. These insights not only clarify the molecular basis of KAND-related R350 mutations but also suggest broader relevance for understanding how microtubule-motor interface integrity contributes to neuronal health.

Methods

This study did not involve human participants or animals and therefore did not require ethical approval.

Generation of plasmids for KIF1A constructs

A plasmid from a previous published KIF1A construct[14] (KIF1A (*Homo sapiens*, aa 1–393)-leucine zipper-SNAPf-EGFP-6His) was used as the template for all constructs in this study. For proteins used in the cryo-EM studies, the SNAPf-EGFP-6His tag was replaced with a strep-II tag (IBA Lifesciences GmbH) using Q5 mutagenesis (New England Biolabs Inc., #E0554S) as in a previous study[20]. Mutations within KIF1A were generated using Q5 mutagenesis. All plasmids were confirmed by Sanger sequencing (Albert Einstein College of Medicine, Genomic Core Facility).

Protein expression in *E. coli*

KIF1A expression was performed as follows: Each plasmid was transformed into BL21-CodonPlus(DE3)-RIPL competent cells (Agilent Technologies, #230280). A single colony was picked and inoculated in 1 mL of terrific broth (TB) (protocol adopted from Cold Spring Harbor protocol[40]) with 50 µg/mL carbenicillin and 50 µg/mL chloramphenicol. The 1-mL culture was shaken at 37 °C overnight and then inoculated into 400 mL of TB (or 1–2 L for cryo-EM studies) with 2 µg/mL carbenicillin and 2 µg/mL chloramphenicol. The culture was shaken at 37 °C for 5 hours and then cooled on ice for 1 hour. Afterwards, IPTG was added to the culture to a final concentration of 0.1 mM and the culture was shaken at 16 °C overnight to induce protein expression. The cells were harvested by centrifugation at 3,000×g for 10 minutes at 4 °C. The supernatant was discarded, and 1.25 mL of B-PER™ Complete Bacterial Protein Extraction Reagent (ThermoFisher Scientific, #89821) per 100 mL culture with 2 mM $MgCl_2$, 1 mM EGTA, 1 mM DTT, 0.1 mM ATP, and 2 mM PMSF was added to the

cell pellet. The cells were fully resuspended, and flash frozen in liquid nitrogen. If the purification was not done on the same day, the frozen cells were stored at –80 °C.

Protein purification

To purify the protein, the frozen cell pellet was thawed at 37 °C. The solution was nutated at room temperature for 20 minutes and then dounced for 10 strokes on ice to lyse the cells. Unless specified, the following procedures were done at 4 °C. The cell lysate was cleared by centrifugation at 80,000 rpm (260,000 × g, *k*-factor=28) for 10 minutes in a TLA-110 rotor using a Beckman Tabletop Ultracentrifuge Unit. The supernatant was flown through 500 µL of Roche cOmplete™ His-Tag purification resin (Millipore Sigma, #5893682001) for His-tag tagged proteins, or 2 mL of Strep-Tactin® 4Flow® high-capacity resin (IBA Lifesciences GmbH, #2-1250-010) for strep-II tagged proteins. The resin was washed with wash buffer (WB) (for His-tagged protein: 50 mM HEPES, 300 mM KCl, 2 mM $MgCl_2$, 1 mM EGTA, 1 mM DTT, 1 mM PMSF, 0.1 mM ATP, 0.1% Pluronic F-127 (w/v), 10% glycerol, pH 7.2; for strep-II tagged protein, Pluronic F-127 and glycerol were omitted). For proteins with a SNAPf-tag, the resin was mixed with 10 µM SNAP-Cell® TMR-Star (New England Biolabs Inc., #S9105S) at room temperature for 10 minutes to label the SNAPf-tag. The resin was further washed with WB, and then eluted with elution buffer (EB) (for His-tagged protein: 50 mM HEPES, 150 mM KCl, 150 mM imidazole, 2 mM $MgCl_2$, 1 mM EGTA, 1 mM DTT, 1 mM PMSF, 0.1 mM ATP, 0.1% Pluronic F-127 (w/v), 10% glycerol, pH 7.2; for strep-II tagged protein: 80 mM PIPES, 2 mM $MgCl_2$, 1 mM EGTA, 1 mM DTT, 0.1 mM ATP, 5 mM desthiobiotin). The Ni-NTA elute was flash frozen and stored at –80 °C. The Strep-Tactin elute was concentrated using a Amicon Ultra-0.5 mL Centrifugal Filter Unit (30-kDa MWCO) (Millipore Sigma, #UFC503024). Storage buffer (SB) (80 mM PIPES, 2 mM $MgCl_2$, 1 mM EGTA, 80% sucrose (w/v)) was added to the protein solution to have a final 20% sucrose (w/v) concentration, and the protein solution was flash frozen and stored at −80 °C. The purity of the proteins was confirmed on polyacrylamide gels (Supplementary Fig. 7).

Microtubule-binding and release assay

A microtubule (MT)-binding and release (MTBR) assay was performed to remove inactive motors for single-molecule TIRF assay. 50 µL of eluted protein was buffer-exchanged into a low salt buffer (30 mM HEPES, 50 mM KCl, 2 mM $MgCl_2$, 1 mM EGTA, 1 mM DTT, 1 mM AMP-PNP, 10 µM taxol, 0.1% Pluronic F-127 (w/v), and 10% glycerol) using 0.5-mL Zeba™ spin desalting column (7-kDa MWCO) (ThermoFisher Scientific, #89882). The solution was warmed to room temperature and 5 µL of

5 mg/mL paclitaxel (Taxol®) stabilized MTs were added. The solution was well mixed and incubated at room temperature for 2 minutes to allow motors to bind to the MTs. Afterward, the solution was spun through a 100 µL glycerol cushion (80 mM PIPES, 2 mM $MgCl_2$, 1 mM EGTA, 1 mM DTT, 10 µM paclitaxel, and 60% glycerol, pH 6.8) by centrifugation at 45,000 rpm (80,000 × g, *k*-factor=33) for 10 minutes at room temperature in TLA-100 rotor using a Beckman Tabletop Ultracentrifuge Unit. Next, the supernatant was removed, and the pellet was resuspended in 50 µL high salt release buffer (30 mM HEPES, 300 mM KCl, 2 mM $MgCl_2$, 1 mM EGTA, 1 mM DTT, 10 µM paclitaxel, 3 mM ATP, 0.1% Pluronic F-127 (w/v), and 10% glycerol). The MTs were then removed by centrifugation at 40,000 rpm (60,000 × g, *k*-factor=41) for 5 minutes at room temperature. Finally, the supernatant containing the active motors was aliquoted, flash frozen in liquid nitrogen, and stored at –80 °C.

Single-molecule TIRF motility assay

MTBR fractions were used for the single-molecule TIRF assay, and the dilutions were adjusted to an appropriate density of motors on MTs. The assay was performed as follows: A flow chamber was assembled with a glass slide (Fisher #12-550-123), an ethanol-cleaned coverslip (Zeiss #474030-9000-000), and two stripes of parafilm. All the following incubation was done at room temperature. 10 µl of 0.5 mg/ml BSA-biotin was flown into the chamber with 10 min incubation. The chamber was then washed with 2×20 µl blocking buffer (80 mM PIPES, 2 mM $MgCl_2$, 1 mM EGTA, 10 µM paclitaxel, 1% Pluronic F-127 (w/v), pH 6.8) and incubated for 10 min to block the surface. Afterwards, 10 µl of 0.25 mg/ml streptavidin was introduced into the chamber with 10 min incubation. The chamber was washed with 2×20 µl blocking buffer, and 10 µl of 0.02 mg/ml Cy5- and biotin-labeled MTs was flown into the chamber with 1 min incubation. The chamber was washed with 2×20 µl blocking buffer. The MTBR motor was diluted in motility buffer (80 mM PIPES, 2 mM $MgCl_2$, 1 mM EGTA, 1 mM DTT, 10 µM paclitaxel, 0.5% Pluronic F-127 (w/v), 2 mM ATP, 5 mg/mL BSA, 1 mg/mL α-casein, gloxy oxygen scavenging system, and 10% glycerol, pH 6.8) in an appropriated dilution, and the solution was introduced into the chamber. The chamber was sealed with vacuum grease. Images were acquired with 200 ms per frame (total 600 frames per movie) and then analyzed via a custom-written MATLAB software. Kymographs were generated using ImageJ2 (version 2.16.0). GraphPad Prism (version 10.4.2) was used to perform statistical analysis and generate graphs.

Single-molecule TIRF apo state binding assay

The concentration of MTBR fractions of the constructs were determined using PAGE. The flow chamber was assembled in the same manner as in motility assay. After the chamber was washed with blocking buffer, the motor was diluted in assay buffer (80 mM PIPES, 200 mM KCl, 2 mM $MgCl_2$, 1 mM EGTA, 1 mM DTT, 10 μM paclitaxel, 0.5% Pluronic F-127 (w/v), 0.01 unit/μL apyrase, 5 mg/mL BSA, 1 mg/mL α-casein, gloxy oxygen scavenging system, and 10% glycerol, pH 7.2) to final 50 pM dimer concentration, and then introduced into the chamber. Image acquisition and analysis were performed as in motility assay. k_{on} was calculated assuming microtubules have 13-protofilaments and each tubulin heterodimer has 8-nm length.

Cryo-EM

Preparation of microtubules

Microtubules (MTs) were prepared from porcine brain tubulin (Cytoskeleton, Inc., CO). Tubulin lyophilized pellets were resuspended in BRB80 (80 mM K-PIPES, 1 mM $MgCl_2$, 1 mM EGTA, pH 6.8) to 5 mg/mL and spun at 313,000 × g before polymerization to eliminate aggregates. MT polymerization was done in conditions to enrich the number of MTs with 15 protofilaments[41] as follows. The clarified resuspended tubulin solution was supplemented with 2 mM GTP, 4 mM $MgCl_2$, 12% (v/v) DMSO and incubated 40 min at 37 °C. An aliquot of stock Paclitaxel (Taxol®) solution (2 mM in DMSO) was added for a final paclitaxel concentration of 250 μM and incubated for another 40 min at 37 °C. The MTs were then spun at 15,500 × g, 25 °C and the pellet resuspended in BRB80 with 20 μM paclitaxel.

Preparation of MT–KIF1A complexes

Four μL of ~6 μM MT solution in BRB80 buffer (80 mM PIPES, 2 mM $MgCl_2$, 1 mM EGTA, pH 6.8) plus 20 μM paclitaxel were layered onto plasma-cleaned grids (Electron Microscopy Sciences, UltrAuFoil R1.2/1.3 300 mesh for ANP samples; R0.6/1 for apo samples). The MTs on the grid were left for 1 minute at room temperature and then the excess liquid was removed using Whatman #1 paper. Four μL of a solution containing either KIF1A-R350G (20 μM) or KIF1A-R350W (17.5 μM) in BRB80 supplemented with 20 μM paclitaxel and either 5 mM AMP-PNP (ANP conditions) or 5×10^{-3} units per μL apyrase (Apo conditions) was then overlaid on the grid with the microtubules. The grids with the MT and kinesin mixture were then mounted into a Vitrobot apparatus (FEI-ThermoFisher, MA), incubated 1 min at room temperature, and plunge-frozen into liquid ethane (Vitrobot settings: 100% humidity, 3 seconds blotting with Whatman #1 paper, and −2 mm offset). Grids were then transferred and stored in liquid nitrogen until data collection.

Cryo-EM data collection

All data were collected on a TF Titan Krios operating at 300 kV and equipped with a Gatan K3 Summit direct electron detector (Gatan, Pleasanton, CA). Data collection was controlled using Leginon[42,43]. Representative micrographs for each construct are shown in Supplementary Fig. 8. The pixel size, defocus range, and total accumulated dose are summarized in Table 1.

Cryo-EM Image analysis and 3D reconstruction

All cryo-EM datasets were processed in CryoSPARC v.4.6.0[44] using an adapted version of the helical single-particle reconstruction and helical assembly subunit refinement/classification (HASRC) workflow[45]. A general overview of the entire workflow is shown in Supplementary Fig. 9. Initial processing for each data set involved patch motion correction and contrast transfer function (CTF) estimation and correction. After micrographs curation, microtubules were manually picked, followed by 2D classification and use of 2D templates to select filament particles using filament tracer. Filament particles were extracted with filament diameter of 350 Å and box size of 664 × 664 pixels. 2D classification of all the filament particles were performed (Supplementary Fig. 10). At this step, class averages corresponding to different microtubule types were distinguished based on their diameter and Moiré pattern[46] and particles corresponding to 15-protofilament microtubules with a right-handed twist (15R) were selected for further processing. Helical refinement was then done with the selected particles using as initial values a helical twist of 168.07°, a helical rise of 5.6 Å, symmetry order of 15 and a maximum out-of-plane tilt of 15° (final twist and rise refined values listed in Table 1). Symmetry expansion was performed using the output parameters from the helical refinement and 15 symmetry order. To reduce computation time, after symmetry expansion the larger datasets were randomly subdivided, and subsets of 4.5 million particles or fewer were selected for further processing. The symmetry expanded dataset were then subjected to signal subtraction to isolate individual protofilaments with associated kinesins. For these, masks encompassing at least 3 tubulin heterodimers and associated kinesins were created. The signal-subtracted single-protofilament reconstruction was locally refined using a mask that encompassed only the tubulin region of the selected protofilament. The resulting 3D reconstruction was then centered and cropped around the isolated protofilament. This dataset was then subsequently subjected to 3D classification to separate classes with and without kinesin decoration, as well as distinct motor domain conformations. For 3D classification, the data were downsampled to a pixel size of ~7.5 Å/pixel using Fourier cropping.

For the ANP datasets, where two-head microtubule-bound states were expected [20], two rounds of classification into six classes were performed. These classifications were performed using masks positioned at the leading and trailing site of the protofilament. Each mask encompassed the volume of a motor domain together with the coiled-coil region, modeled in the "up" (at the plus-end of the mask volume) and in the "down" positions (at the minus-end of the mask volume). For MT-KIF1A-R350G-ANP, the initial round used a trailing site mask with the coiled-coil modeled in the "down" position, followed by a subsequent round using a leading site mask with the coiled-coil in the "up" position. From the trailing site classification, four of six classes were regrouped and subjected to leading site classification, and two of the resulting six classes were used to generate the final locally refined volume (Supplementary Fig. 11a). For MT-KIF1A-R350W-ANP, the initial round used a mask positioned at the leading site of the protofilament, and the subsequent round used a mask at the trailing site. This yielded classes corresponding to: (i) leading-like configurations, with coiled-coil densities in the down position; (ii) trailing-like configurations, with coiled-coil densities in the up position; (iii) empty classes with no discernible kinesin densities; and (iv) noisy classes that could not be confidently assigned as leading, trailing, or empty (Supplementary Fig. 11b). Particles classified as leading at the leading position and trailing at the trailing position were selected for the final 3D reconstruction. using the Particle Sets tool.

For the apo datasets, only one round of 3D classification was performed on a single kinesin motor domain position, given that in the apo state only one-head–microtubule-bound conformations are expected [20]. This was further supported by the helical reconstructions, which likewise indicated that these datasets correspond to kinesins with only one microtubule-bound head, with no neck coiled-coil densities. The MT-KIF1A-R350G-apo dataset was classified into six classes (Supplementary Fig. 11c) and the MT-KIF1A-R350W-apo into 10 classes (Supplementary Fig. 11d). The 3D classification step yielded classes showing either kinesin-bound densities, noise, or empty sites. After 3D classification, the selected particle poses were used to generate a 3D volume at the original pixel size (i.e., not downsampled), and these volumes were then locally refined. Masks for local refinement, 3D classification, and inverse masks for particle subtraction were generated from low-resolution (30 Å) density maps based on atomic models of kinesin-decorated protofilaments. These were produced using the molmap function in UCSF Chimera 1.47, and then imported, thresholded, and inverted (for particle subtraction) using the CryoSPARC volume import and volume tools.

Model building and model refinement

Initial models PDB 8UTN and PDB 8UTS[20] were fitted into the ANP and apo maps, respectively, using the *Fit in Map* function in UCSF-Chimera[47]. Mutations at residue R350 were introduced in Coot[48], replacing it with glycine (R350G) or tryptophan (R350W). These initial mutated models for each of the four complexes were flexibly fitted into their respective cryo-EM maps using Rosetta refinement protocols[49]. Models with the best agreement to the cryo-EM density and best Molprobity[50] scores were selected and further refined using Phenix real-space refinement[51]. Refined models were then manually edited using Coot[48] and ISOLDE[52]. Several rounds of manual editing and Phenix real-space refinement were performed until the final models were obtained. Figures of the atomic models and cryo-EM maps were prepared using UCSF-Chimera[47] and UCSF-ChimeraX[53].

Model coordinate precision

The precision of atomic coordinates in the fitted cryo-EM models was estimated using the method proposed by Herzik *et al.*[54]. For each map and fitted model, 40 additional models were generated via flexible fitting with Rosetta[49]. The ten best-scoring models, based on density fit and MolProbity scores, together with the original model, were used to assess coordinate variation. Precision was expressed as the RMSD between equivalent Cα atoms across the 11 models (Supplementary Fig. 2).

Statistics and reproducibility

Data are presented as mean ± s.d. or mean ± s.e.m., as indicated in the figure legends, together with n values. Statistical analyses were performed using unpaired two-tailed Student's t-test or Kolmogorov–Smirnov test, as appropriate, with P values calculated in GraphPad Prism. No statistical method was used to predetermine sample size. No data were excluded from the analyses. The experiments were not randomized, and investigators were not blinded to allocation during data collection or analysis.

Sample size estimation, randomization, and blinding were not applicable to this study. The experiments are based on in vitro biochemical assays, single-molecule measurements, and cryo-EM image analysis, where there is no allocation of biological subjects into experimental groups. Rather, comparisons are made between predefined experimental conditions (e.g., protein variants or nucleotide states), and sample size reflects the number of independent experimental replicates or particles contributing to each condition. Data collection and analysis rely on standardized and largely automated computational

workflows, minimizing subjective bias. Structural and quantitative conclusions were supported by independent datasets and established validation metrics.

Data availability

The data that support this study are available from the corresponding authors upon request. The atomic coordinates have been deposited in the Protein Data Bank (PDB) under accession codes 9YA5 [https://doi.org/10.2210/pdb9YA5.pdb]; 9YAI [https://doi.org/10.2210/pdb9YAI.pdb]; 9YA7 [https://doi.org/10.2210/pdb9YA7.pdb]; and 9YAB [https://doi.org/10.2210/pdb9YAB.pdb]. Corresponding cryo-EM maps, half maps, FSC curves and masks used have been deposited in the Electron Microscopy Data Base (EMDB) with accession codes: EMD-72721 [https://www.ebi.ac.uk/emdb/EMD-72721], EMD-72728 [https://www.ebi.ac.uk/emdb/EMD-72728], EMD-72723 [https://www.ebi.ac.uk/emdb/EMD-72723], and EMD-72726 [https://www.ebi.ac.uk/emdb/EMD-72726]. The previously published structural models PDB ids: 7WRG [https://doi.org/10.2210/pdb7wrg/pdb]; 8UTN [https://doi.org/10.2210/pdb8UTN/pdb]; 8UTO [https://doi.org/10.2210/pdb8UTO/pdb]; 8UTP [https://doi.org/10.2210/pdb8UTP/pdb]; and 8UTS [https://doi.org/10.2210/pdb8UTS/pdb] were referenced in this work.

References

1. Hall, D.H. & Hedgecock, E.M. Kinesin-related gene unc-104 is required for axonal transport of synaptic vesicles in C. elegans. *Cell* **65**, 837-847 (1991).
2. Okada, Y., Yamazaki, H., Sekine-Aizawa, Y. & Hirokawa, N. The neuron-specific kinesin superfamily protein KIF1A is a unique monomeric motor for anterograde axonal transport of synaptic vesicle precursors. *Cell* **81**, 769-80. (1995).
3. Yonekawa, Y. et al. Defect in Synaptic Vesicle Precursor Transport and Neuronal Cell Death in KIF1A Motor Protein–deficient Mice. *Journal of Cell Biology* **141**, 431-441 (1998).
4. Zahn, T.R. et al. Dense Core Vesicle Dynamics in Caenorhabditis elegans Neurons and the Role of Kinesin UNC-104. *Traffic* **5**, 544-559 (2004).
5. Barkus, R.V., Klyachko, O., Horiuchi, D., Dickson, B.J. & Saxton, W.M. Identification of an Axonal Kinesin-3 Motor for Fast Anterograde Vesicle Transport that Facilitates Retrograde Transport of Neuropeptides. *Molecular Biology of the Cell* **19**, 274-283 (2008).
6. Lo, K.Y., Kuzmin, A., Unger, S.M., Petersen, J.D. & Silverman, M.A. KIF1A is the primary anterograde motor protein required for the axonal transport of dense-core vesicles in cultured hippocampal neurons. *Neuroscience Letters* **491**, 168-173 (2011).
7. Carabalona, A., Hu, D.J.-K. & Vallee, R.B. KIF1A inhibition immortalizes brain stem cells but blocks BDNF-mediated neuronal migration. *Nature Neuroscience* **19**, 253-262 (2016).

8. Tsai, J.-W., Lian, W.-N., Kemal, S., Kriegstein, A.R. & Vallee, R.B. Kinesin 3 and cytoplasmic dynein mediate interkinetic nuclear migration in neural stem cells. *Nature Neuroscience* **13**, 1463-1471 (2010).
9. Yildiz, A. Mechanism and regulation of kinesin motors. *Nature Reviews Molecular Cell Biology* (2024).
10. Siddiqui, N. & Straube, A. Intracellular cargo transport by kinesin-3 motors. *Biochemistry (Moscow)* **82**, 803-815 (2017).
11. Tomishige, M., Klopfenstein, D.R. & Vale, R.D. Conversion of Unc104/KIF1A kinesin into a processive motor after dimerization. *Science* **297**, 2263-7 (2002).
12. Soppina, V. et al. Dimerization of mammalian kinesin-3 motors results in superprocessive motion. *Proceedings of the National Academy of Sciences* **111**, 5562-5567 (2014).
13. Hammond, J.W. et al. Mammalian Kinesin-3 Motors Are Dimeric In Vivo and Move by Processive Motility upon Release of Autoinhibition. *PLOS Biology* **7**, e1000072 (2009).
14. Boyle, L. et al. Genotype and defects in microtubule-based motility correlate with clinical severity in KIF1A-associated neurological disorder. *Human Genetics and Genomics Advances* **2**, 100026 (2021).
15. Nair, A. et al. KIF1A-Associated Neurological Disorder: An Overview of a Rare Mutational Disease. *Pharmaceuticals (Basel)* **16**(2023).
16. Kaur, S. et al. Local computational methods to improve the interpretability and analysis of cryo-EM maps. *Nature Communications* **12**, 1240 (2021).
17. Budaitis, B.G. et al. Pathogenic mutations in the kinesin-3 motor KIF1A diminish force generation and movement through allosteric mechanisms. *Journal of Cell Biology* **220**(2021).
18. Lam, A.J. et al. A highly conserved 3₁₀ helix within the kinesin motor domain is critical for kinesin function and human health. *Science Advances* **7**, eabf1002 (2021).
19. Anazawa, Y., Kita, T., Iguchi, R., Hayashi, K. & Niwa, S. De novo mutations in KIF1A-associated neuronal disorder (KAND) dominant-negatively inhibit motor activity and axonal transport of synaptic vesicle precursors. *Proceedings of the National Academy of Sciences* **119**, e2113795119 (2022).
20. Benoit, M.P.M.H., Rao, L., Asenjo, A.B., Gennerich, A. & Sosa, H. Cryo-EM unveils kinesin KIF1A's processivity mechanism and the impact of its pathogenic variant P305L. *Nature Communications* **15**, 5530 (2024).
21. Rao, L., Li, W., Shen, Y., Chung, W.K. & Gennerich, A. Distinct Clinical Phenotypes in KIF1A-Associated Neurological Disorders Result from Different Amino Acid Substitutions at the Same Residue in KIF1A. *Biomolecules* **15**, 656 (2025).
22. Chiba, K. et al. Disease-associated mutations hyperactivate KIF1A motility and anterograde axonal transport of synaptic vesicle precursors. *Proceedings of the National Academy of Sciences* **116**, 18429-18434 (2019).
23. Chiba, K., Kita, T., Anazawa, Y. & Niwa, S. Insight into the regulation of axonal transport from the study of KIF1A-associated neurological disorder. *Journal of Cell Science* **136**(2023).
24. Klebe, S. et al. KIF1A missense mutations in SPG30, an autosomal recessive spastic paraplegia: distinct phenotypes according to the nature of the mutations. *European Journal of Human Genetics* **20**, 645-649 (2012).
25. Rice, S. et al. A structural change in the kinesin motor protein that drives motility. *Nature* **402**, 778-784 (1999).

26. Lee, J.-R. et al. De Novo Mutations in the Motor Domain of KIF1A Cause Cognitive Impairment, Spastic Paraparesis, Axonal Neuropathy, and Cerebellar Atrophy. *Human Mutation* **36**, 69-78 (2015).
27. Sosa, H. et al. A model for the microtubule-Ncd motor protein complex obtained by cryo-electron microscopy and image analysis. *Cell* **90**, 217-224 (1997).
28. Woehlke, G. et al. Microtubule interaction site of the kinesin motor. *Cell* **90**, 207-16 (1997).
29. Hoenger, A. et al. Image reconstructions of microtubules decorated with monomeric and dimeric kinesins: comparison with x-ray structure and implications for motility. *Journal of Cell Biology* **141**, 419-30 (1998).
30. Kikkawa, M., Okada, Y. & Hirokawa, N. 15 A resolution model of the monomeric kinesin motor, KIF1A. *Cell* **100**, 241-52. (2000).
31. Hirose, K., Akimaru, E., Akiba, T., Endow, S.A. & Amos, L.A. Large conformational changes in a kinesin motor catalyzed by interaction with microtubules. *Mol Cell* **23**, 913-23 (2006).
32. Sindelar, C.V. & Downing, K.H. The beginning of kinesin's force-generating cycle visualized at 9-A resolution. *J Cell Biol* **177**, 377-85 (2007).
33. Uchimura, S., Oguchi, Y., Hachikubo, Y., Ishiwata, S.i. & Muto, E. Key residues on microtubule responsible for activation of kinesin ATPase. *The EMBO Journal* **29**, 1167-1175 (2010).
34. Benoit, M.P.M.H., Hunter, B., Allingham, J.S. & Sosa, H. New insights into the mechanochemical coupling mechanism of kinesin–microtubule complexes from their high-resolution structures. *Biochemical Society Transactions* **51**, 1505-1520 (2023).
35. Aguilera, C. et al. The Novel KIF1A Missense Variant (R169T) Strongly Reduces Microtubule Stimulated ATPase Activity and Is Associated With NESCAV Syndrome. *Frontiers in Neuroscience* **15**(2021).
36. Li, M. & Zheng, W. Probing the Structural and Energetic Basis of Kinesin–Microtubule Binding Using Computational Alanine-Scanning Mutagenesis. *Biochemistry* **50**, 8645-8655 (2011).
37. Torella, A. et al. A new genetic cause of spastic ataxia: the p.Glu415Lys variant in TUBA4A. *Journal of Neurology* **270**, 5057-5063 (2023).
38. Wang, W., Ren, J., Song, W., Zhang, Y. & Feng, W. The architecture of kinesin-3 KLP-6 reveals a multilevel-lockdown mechanism for autoinhibition. *Nature Communications* **13**, 4281 (2022).
39. Abramson, J. et al. Accurate structure prediction of biomolecular interactions with AlphaFold 3. *Nature* **630**, 493-500 (2024).
40. Terrific Broth. *Cold Spring Harbor Protocols* **2006**, pdb.rec8620 (2006).
41. Wilson-Kubalek, E.M., Cheeseman, I.M. & Milligan, R.A. Structural comparison of the Caenorhabditis elegans and human Ndc80 complexes bound to microtubules reveals distinct binding behavior. *Mol Biol Cell* **27**, 1197-203 (2016).
42. Cheng, A. et al. Fully automated multi-grid cryoEM screening using Smart Leginon. *IUCrJ* **10**, 77-89 (2023).
43. Suloway, C. et al. Automated molecular microscopy: The new Leginon system. *Journal of Structural Biology* **151**, 41-60 (2005).
44. Punjani, A., Rubinstein, J.L., Fleet, D.J. & Brubaker, M.A. cryoSPARC: algorithms for rapid unsupervised cryo-EM structure determination. *Nature Methods* **14**, 290-296 (2017).
45. Benoit, M.P.M.H. et al. Structural basis of mechano-chemical coupling by the mitotic kinesin KIF14. *Nature Communications* **12**, 3637 (2021).
46. Sosa, H. & Milligan, R.A. Three-Dimensional Structure of Ncd-Decorated Microtubules Obtained By a Back-Projection Method. *Journal of Molecular Biology* **260**, 743-755 (1996).

47. Pettersen, E.F. et al. UCSF Chimera--a visualization system for exploratory research and analysis. *J Comput Chem* **25**, 1605-12 (2004).
48. Emsley, P. & Cowtan, K. Coot: model-building tools for molecular graphics. *Acta Crystallographica Section D* **60**, 2126-2132 (2004).
49. DiMaio, F., Tyka, M.D., Baker, M.L., Chiu, W. & Baker, D. Refinement of Protein Structures into Low-Resolution Density Maps Using Rosetta. *Journal of Molecular Biology* **392**, 181-190 (2009).
50. Williams, C.J. et al. MolProbity: More and better reference data for improved all-atom structure validation. *Protein Science* **27**, 293-315 (2018).
51. Afonine, P.V. et al. Real-space refinement in PHENIX for cryo-EM and crystallography. *Acta Crystallographica Section D* **74**, 531-544 (2018).
52. Croll, T. ISOLDE: a physically realistic environment for model building into low-resolution electron-density maps. *Acta Crystallographica Section D* **74**, 519-530 (2018).
53. Goddard, T.D. et al. UCSF ChimeraX: Meeting modern challenges in visualization and analysis. *Protein Science* **27**, 14-25 (2018).
54. Herzik, M.A., Fraser, J.S. & Lander, G.C. A Multi-model Approach to Assessing Local and Global Cryo-EM Map Quality. *Structure* **27**, 344-358.e3 (2019).

Acknowledgements

This work was supported by the National Institutes of Health Grant R01GM147332 (A.G and H.S), R01GM113164 (H.S.). Cryo-EM data collection was performed at the Simons Electron Microscopy Center and National Resource for Automated Molecular Microscopy located at the New York Structural Biology Center, supported by grants from the Simons Foundation (SF349247), NYSTAR, and the NIH National Institute of General Medical Sciences (GM103310) with additional support from Agouron Institute (F00316) and NIH (OD019994). We thank Wendy Chung for helpful discussions on disease severity of KAND-associated R350 mutations.

Author Contributions

A.S. processed the cryo-EM data; built, fitted, and refined the atomic models. L.R. generated, expressed, and purified the constructs for the cryo-EM and single-molecule studies. L.R. performed the single-molecule experiments, collected and analyzed the data, and interpreted the results. A.S., A.B.A., and H.S. designed the cryo-EM experiments. A.S. and A.B.A. assembled kinesin–microtubule complexes and prepared cryo-EM grids. A.S. and A.B.A. performed sample screening and optimization for cryo-EM imaging and selected microtubules for data collection. A.G. and H.S. conceived and coordinated the project and interpreted the results. A.S., L.R., A.B.A., A.G., and H.S. wrote and edited the manuscript.

Competing Interests Statement

The authors declare no competing interests

Table and Fig. Legends

Table 1: Cryogenic Electron Microscopy Data Collection, Coordinate Refinement and Validation Statistics

Fig. 1 Cryo-EM maps of mutant KIF1A bound to microtubules in the ANP-bound and apo states. Iso-surface representation of the 3D reconstruction of microtubule-bound **a** KIF1A-R350G in the ANP-bound state. **b** KIF1A-R350W in the ANP-bound state. **c** KIF1A-R350G in the apo state. **d** KIF1A-R350W in the apo state. Surface coloring highlights distinct structural elements: the KIF1A core motor domain (teal), Loop-12/K-loop (L12, magenta), neck-linker (red), coiled-coil (CC, yellow), ANP (orange), Loop-9/switch-1 (L9, green), helix-0 (H0, purple), α-tubulin (light gray), and β-tubulin (gray). Cryo-EM densities corresponding to less-resolved, more mobile regions such as the tip of the K-loop, part of the leading neck-linker, and the coiled-coil were low-pass filtered and are shown as semitransparent iso-surfaces.

Fig. 2 Comparison of KIF1A R350G and R350W mutants in the two-heads-bound ANP state. Superimposed models of KIF1A-R350G-ANP (red) and KIF1A-R350W-ANP (green) are shown. The two models were aligned to their respective leading motor domains, highlighting the different relative positions between the leading and trailing heads in the two mutants. The inset shows a close-up of a region in the motor domain (helix H2) with associated cryo-EM densities, illustrating the distinct relative positions of the densities and fitted models. Cryo-EM densities are displayed as iso-contour mesh surfaces. α- and β-tubulin are shown in light gray and gray, respectively. The figure is oriented with the microtubule plus-end to the right.

Fig. 3 | KIF1A motor domain structures of wild-type and R350 mutants. a Nucleotide pocket (NP) openness, expressed as the average distance between highly conserved residues across the nucleotide-binding pocket (R216 and A250 to P14, S104 and Y105; inset). Bar heights and error bars indicate the mean ± s.d. of openness values derived from alternative fitted models used to estimate coordinate precision (Supplementary Fig. 2). Wild-type values were taken from ref[20] (PDB IDs: 8UTS, 8UTN, 8UTP and 8UTO). *n* values for each dataset (left to right) are 6, 11, 11, 18, 11, 11, 18, 11 and 11. **b–d** Structural alignment of MT-KIF1A-WT (blue), MT-KIF1A-R350G (red) and MT-KIF1A-R350W (green) motor domains in the apo state (b), the leading head of the AMP-PNP–bound state (c) and the

trailing head of the AMP-PNP–bound state (d). α- and β-tubulin are shown in light and dark grey, respectively. In b–d, models are oriented with the microtubule plus end to the left.

Fig. 4 Structures of microtubule-bound KIF1A WT and R350 mutants near residue 350. **a–c** WT. **d–f** R350G. **g–i** R350W. Apo state, open conformation (a, d, g); ANP state, leading-head open conformation (b, e, h); ANP state, trailing-head closed conformation (c, f, i). Model structures are shown in atom-stick representation. KIF1A motor domain in teal, with residue 350 colored by heteroatom and its carbon backbone in ochre. α-Tubulin is shown in light gray, with residue E415 colored by heteroatom and its carbon backbone in blue. Hydrogen bonds between KIF1A WT R350 and α-tubulin E415 are indicated as dashed purple lines (a, b). Corresponding cryo-EM densities are shown as semi-transparent gray mesh iso-surfaces. WT structures correspond to PDB IDs 8UTS (a) and 8UTN (b–c) after molecular dynamics fitting with ISOLDE[52].

Fig. 5 Single-molecule microtubule-binding of WT KIF1A and R350 mutants in the apo state. a Examples of kymographs of KIF1A WT, R350G, and R350W at apo state in the presence of 200 mM KCl. **b** k_{on} and k_{off} of KIF1A WT, R350G, and R350W binding to microtubules in the presence of 200 mM KCl at 50 pM concentration. Each data point represents the average k_{on} or k_{off} from a technical replicate (total 3 replicates for each construct). Error bars represent mean value ± SEM. k_{on}: WT: 11.1 ± 1.1 × 10^4 M^{-1} s^{-1}; R350G: 6.9 ± 0.9 × 10^4 M^{-1} s^{-1}; R350W: 3.2 ± 0.3 × 10^4 M^{-1} s^{-1}. Statistical analysis was performed with one-way ANOVA using WT as control. *: P=0.0235; **: P=0.0011. k_{off}: WT: 0.055 ± 0.003 s^{-1}; R350G: 0.138 ± 0.018 s^{-1}; R350W: 0.419 ± 0.023 s^{-1}. Statistical analysis was performed with one-way ANOVA using WT as control. *: P=0.0170; ****: P<0.0001. **c** Dwell time of all the events combined was fit with one-phase exponential decay. Fitted k_{off} values are shown in (d). d The summary table of k_{on}, k_{off} (from (c)), K_D, and ΔG.

Fig. 6 Single-molecule motility of KIF1A WT and R350 mutants. a Examples of kymographs of KIF1A WT, R350G, and R350W. b Left panel: velocity of KIF1A WT, R350G, and R350W. The green bars indicate median value with 95% confidence interval (CI). WT: 2.43 [2.41, 2.45] μm/s, n=330. R350G: 2.67 [2.64, 2.71] μm/s, n=354. R350W: 2.59 [2.56, 2.62] μm/s, n=673. A Welch's t-test was performed to compare the velocity distributions. P value: ****, P<0.0001; ns, P=0.0774. Right panel: Processivity of KIF1A WT, R350G, and R350W. The green bars indicate median value with 95%

confidence interval (CI). The numbers of data points are the same as the velocity plot. WT: 16.7 [15.5, 17.6] μm. R350G: 9.0 [8.1, 10.0] μm. R350W: 5.3 [4.9, 5.7] μm. A Kolmogorov-Smirnov test was performed to compare the run-length distributions. ****, P<0.0001. All statistical tests were two-tailed.

Fig. 7 Graphical summary. KIF1A residue R350 forms a salt bridge with α-tubulin E415 in the open conformation of the motor domain. Disruption of this salt bridge in the R350G and R350W mutants facilitates conversion to the closed state, with neck-linker docking and forward movement of the partner motor domain to the leading position (step 1), resulting in increased translocation velocity. Conversely, disruption of the salt bridge also increases the likelihood of microtubule detachment (step 2), leading to reduced processivity. KIF1A motor domain is shown in blue, neck-linker in red, neck coiled coil in green, α-tubulin in light gray, and β-tubulin in dark gray. The microtubule plus end is oriented to the right.

Dataset	**MT-KIF1A-R350G-ANP**	**MT-KIF1A-R350W-ANP**	**MT-KIF1A-R350G-apo**	**MT-KIF1A-R350W-apo**
PDB	9YA5	9YAI	9YA7	9YAB
EMDB	72721	72728	72723	72726
Data collection and processing				
Microscope	EF-Krios	EF-Krios	EF-Krios	EF-Krios
Voltage (kV)	300	300	300	300
Camera	Gatan K3	Gatan K3	Gatan K3	Gatan K3
Magnification	81000	64000	105000	105000
Defocus range (um)	-0.6 to -2.5	-0.8 to -2.5	-0.5 to -2.3	-0.1 to -2.3
Exposure time (ms)	1200	2000	1001	1320
Electron dose ($e^-/Å^2$)	50.27	52.14	52.88	57.96
Calibrated pixel size (Å)	0.8460	1.0730	0.8260	0.8260
Revised pixel size (Å) of the final map	0.8791	-	-	-
Symmetry imposed	Helical	Helical	Helical	Helical
Rise (Å)	5.453	5.536	5.562	5.571
Twist (deg)	168.07	168.07	168.07	168.07
Initial particle images after symmetry expansion (no.)	5,286,915	13,174,335	4,318,200	2,376,645
Final particle images (no.)	1,194,267	556,086	4,318,200	953,398
Overall Map resolution (Å), 0.143 FSC	2.94	3.14	3.33	3.20
Tubulin resolution (Å)	2.89	3.10	3.33	3.17
Kinesin resolution (Å), Coiled coil excluded	3.17	3.32	4.03	4.16
Map sharpening B-factor ($Å^2$)	84.3	85.3	114.1	104.8
Refinement				
Model composition				
Non-hydrogen atoms	19724	19749	9703	9687
Protein residues	2475	2478	1222	1219
Ligands	11	11	4	4
B factors ($Å^2$)				
Protein	119.65	114.60	107.89	88.32
Ligand	123.36	120.94	111.16	84.16
RMS deviations				
Bond lengths (Å)	0.006	0.006	0.004	0.005
Bond angles (°)	1.170	1.154	0.903	1.108

Validation				
MolProbity score	1.38	1.48	1.32	1.13
Clash score	1.60	3.16	1.99	1.21
Rotamer outliers (%)	1.74	1.41	1.52	0.95
Ramachandran plot				
Favored (%)	95.85	96.23	96.63	95.79
Allowed (%)	4.11	3.73	3.37	4.21
Outliers (%)	0.04	0.04	0.00	0.00

Distinct KIF1A mutations cause neurological disease, but the mechanism for many variants remains unclear. Here, the authors use cryo-EM and motility assays to show that R350 mutations disrupt a conserved, conformation-dependent kinesin–tubulin salt bridge, altering motor function.

Peer review information: *Nature Communications* thanks Robert Cross, who co-reviewed with Vishakha Karnawat, and the other, anonymous, reviewer(s) for their contribution to the peer review of this work. A peer review file is available.

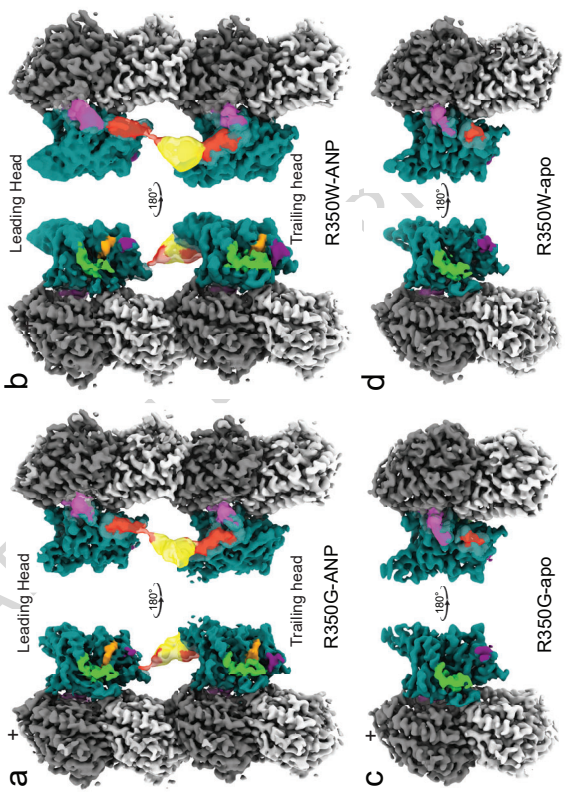
a
+
Leading Head
180°
Trailing head
R350G-ANP
b
Leading Head
180°
Trailing head
R350W-ANP
c
+
180°
R350G-apo
d
180°
R350W-apo

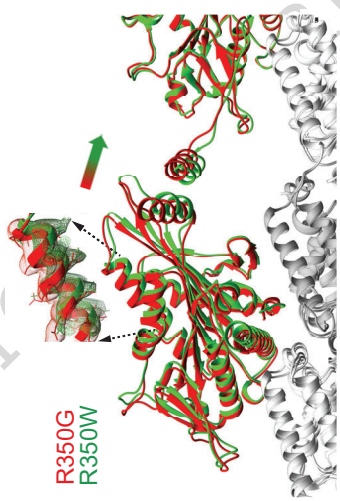

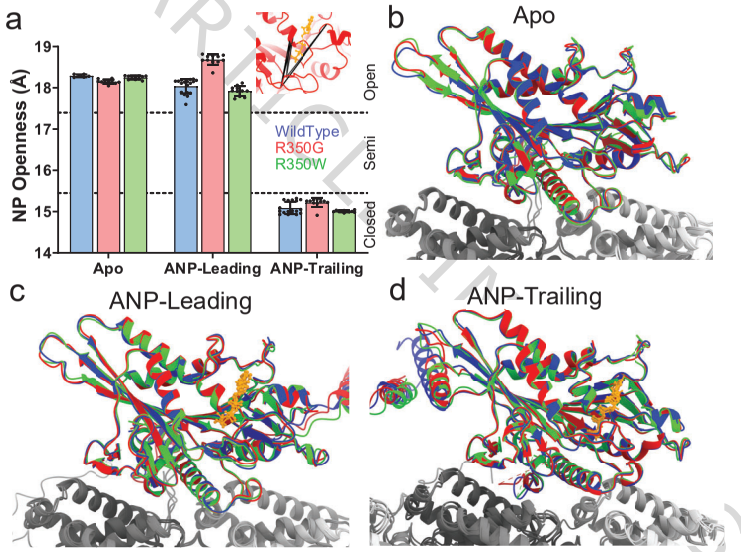

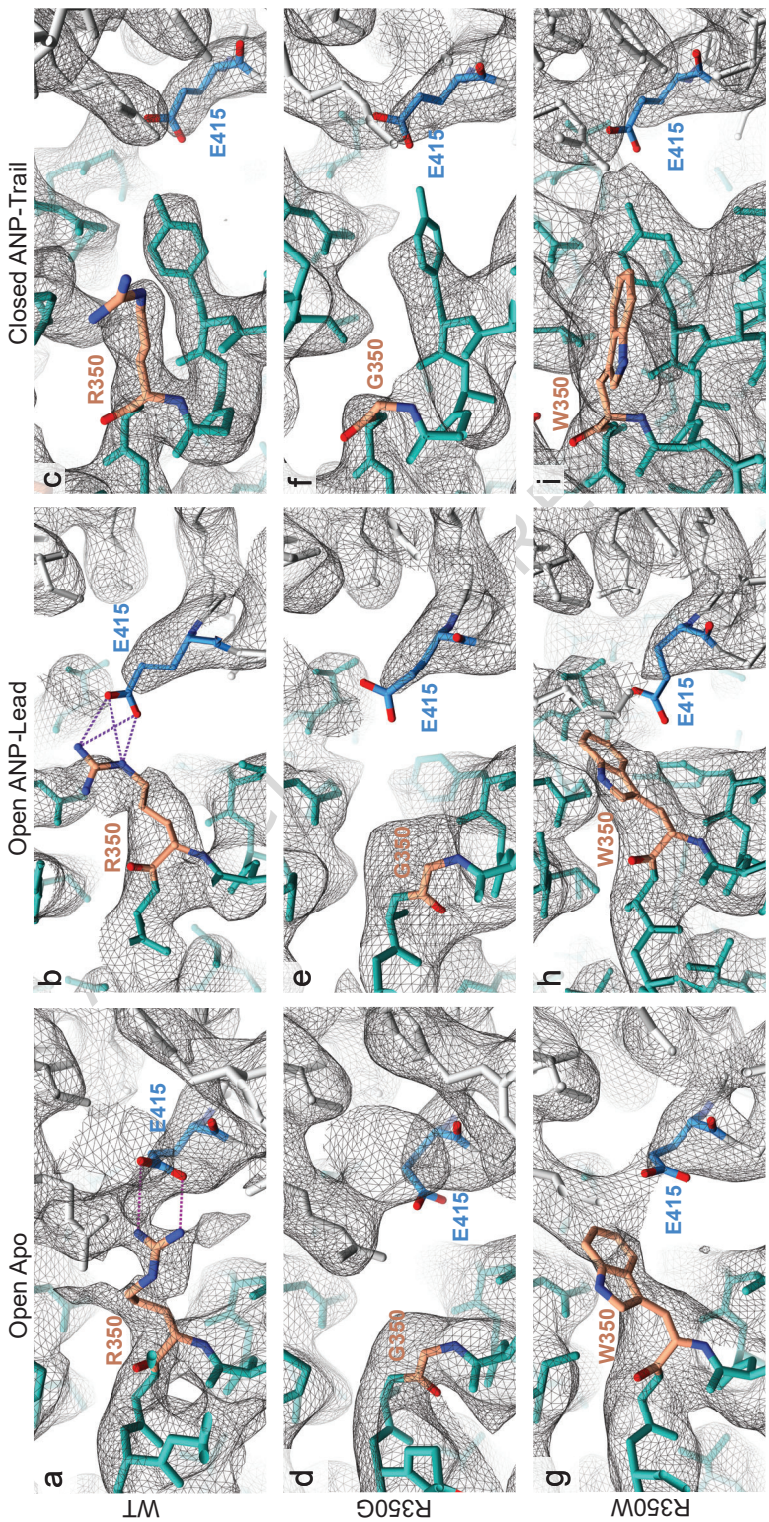
Open Apo
Open ANP-Lead
Closed ANP-Trail
WT
R350G
R350W
a
b
c
d
e
f
g
h
i
R350
G350
W350
E415

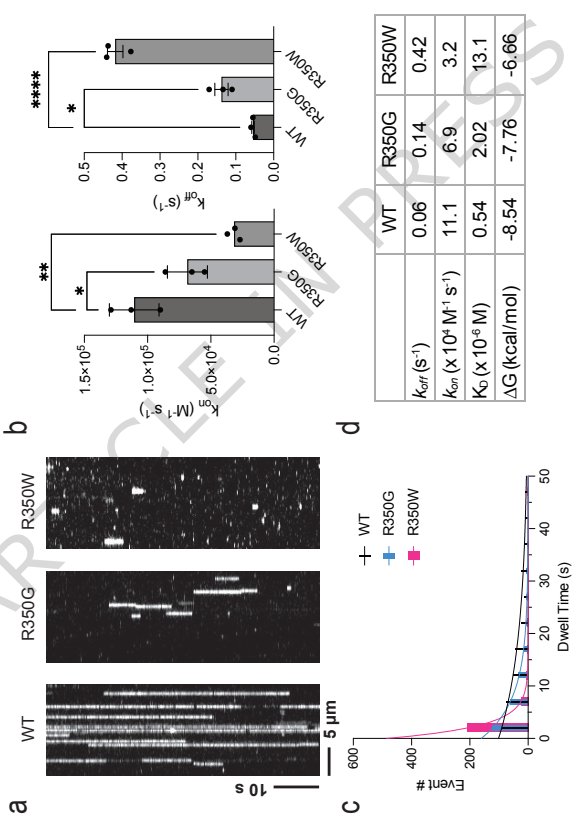

d

	WT	R350G	R350W
k_{off} (s^{-1})	0.06	0.14	0.42
k_{on} (x 10^4 M^{-1} s^{-1})	11.1	6.9	3.2
K_D (x 10^{-6} M)	0.54	2.02	13.1
ΔG (kcal/mol)	-8.54	-7.76	-6.66